ACS OMEGA

http://pubs.acs.org/journal/acsodf

Article

Structural Characterization of Human Histone H4.1 by Tandem Nonlinear and Linear Ion Mobility Spectrometry Complemented with Molecular Dynamics Simulations

Khoa N. Pham and Francisco Fernandez-Lima*

Cite This: *ACS Omega* 2021, 6, 29567−29576

Read Online

ACCESS | Metrics & More | Article Recommendations | Supporting Information

ABSTRACT: Extracellular histone H4 is an attractive drug target owing to its roles in organ failure in sepsis and other diseases. To identify inhibitors using in silico methods, information on histone H4 structural dynamics and three-dimensional (3D) structural coordinates is required. Here, DNA-free histone H4 type 1 (H4.1) was characterized by utilizing tandem nonlinear and linear ion mobility spectrometry (FAIMS-TIMS) coupled to mass spectrometry (MS) complemented with molecular dynamics (MD) simulations. The gas-phase structures of H4.1 are dependent on the starting solution conditions, evidenced by differences in charge state distributions, mobility distributions, and collision-induced unfolding (CIU) pathways. The experimental results show that H4.1 adopts diverse conformational types from compact (C) to partially folded (P) and subsequently elongated (E) structures. Molecular dynamics simulations provided candidate structures for the histone H4.1 monomer in solution and for the gas-phase structures observed using FAIMS-IMS-TOF MS as a function of the charge state and mobility distribution. A combination of the FAIMS-TIMS experimental results with theoretical dipole calculations reveals the important role of charge distribution in the dipole alignment of H4.1 elongated structures at high electric fields. A comparison of the secondary and primary structures of DNA-free H2A.1 and H4.1 is made based on the experimental IMS-MS and MD findings.

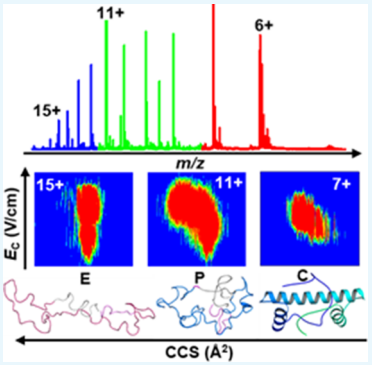

INTRODUCTION

Histones are intrinsically disordered proteins[1] that package eukaryotic DNA into nucleosomes within cell nuclei.[2,3] A nucleosome consists of 147 base pairs of DNA wrapped around an octameric core histone comprising two pairs of each heterodimer of histones H3 and H4 and histones H2A and H2B.[2,3] A nucleosome is connected to its adjacent nucleosome by a DNA segment associated with a linker histone H1 or H5 to form chromatin fiber.[4] A core histone contains a central helix fold and an intrinsically disordered and charged N-terminal tail, which is protruded from the nucleosome and is highly subjected to post-translational modifications (PTMs) such as acetylation, methylation, phosphorylation, and glycosylation.[2,5,6] The functions of histone PTMs are of particular interest and have been investigated extensively because combinatorial PTMs create "histone codes"[5] that regulate DNA transcriptional activity,[5,7] DNA replication,[5] DNA repair, and recombination.[8] Moreover, alterations in patterns of histone PTMs have been related to deregulation of the expression of many genes having crucial functions in cancer development and progression.[6,9] During cell metabolism, newly synthesized DNA-free histones in the cytoplasm are transported into the nucleus by chaperones for replacement of old/damaged histones.[10] Histones can be released into the extracellular space after significant cellular death such as sepsis, trauma, ischemia-reperfusion injury, and autoimmune disease.[11] Once entered the extracellular space, histones function as damage-associated molecular pattern proteins, triggering the immune system and causing cytotoxicity.[11] Extracellular histones can be found in a form of nucleosome-containing structures, neutrophil extracellular traps (NETs, comprising ∼70% histones), or DNA-free histones.[12] Degradation of NETs and nucleosomes in the bloodstream releases DNA-free histones, which are cytotoxic due to their highly cationic nature.[12] Recent studies have shown that DNA-free histones play important roles in organ failure and death in sepsis and other diseases.[12−14] In addition, a study in COVID-19 patients showed a correlation of the serum-citrullinated histone H3 level with acute respiratory distress syndrome.[12,15] Moreover, it has been reported that histone H4 functions as a mediator causing arterial tissue damage and inflammation.[16] Furthermore, histone H4 also induces platelet aggregation in thrombocytopenia.[17] These studies imply a new trending strategy in the discovery of novel drugs that effectively inhibit the release of histones and/or neutralize circulating histones.

Received: July 14, 2021
Accepted: October 15, 2021
Published: October 27, 2021

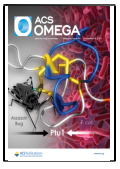

Recently, small polyanions[12] and peptidic inhibitors[18] have been developed, targeting electrostatic interactions with histone H4 and H2A monomers to neutralize their pathological effects. The successes of these studies represent a promise for the development of inhibitors targeting intrinsically disordered histone monomers.[18] With the advent of advanced molecular modeling software, in silico drug discovery approaches have been successfully applied for identification of potential lead inhibitors before extensive experimental assays.[19] To identify inhibitors using in silico methods, information on the protein intrinsic dynamics and their three-dimensional (3D) structures is required.[18,20] However, the structural analysis and 3D structures of the H4.1 monomer are currently absent. Furthermore, for efficient identification and design of inhibitors for histone monomers using in silico approaches, a proper understanding of biomolecular recognition mechanisms is needed.[18,20] For instance, protein flexibility such as conformational changes prior and upon association with inhibitors is diverse and not obvious when only a few or no protein structures are available.[20] In addition, using one protein conformation for structure-based screening restricts the chemical space of potential inhibitors for a specific drug target. Therefore, an ensemble of protein structures needs to be exploited to improve the accuracy.[20]

In this paper, we applied the recently developed methods and strategies for successful structural analysis of an intrinsically disordered histone H2A.1[21] to characterize the gas-phase structures of human histone H4.1. Briefly, in nonlinear ion mobility spectroscopy (i.e., field asymmetric IMS, FAIMS), ion mobilities are separated based on different K values (ΔK) between the low and high electric fields (E),[22,23] whereas in linear IMS, particularly trapped IMS (TIMS), ion mobilities are measured based on the rotationally averaged collision cross section (CCS).[24,25] The IMS-mass spectrometry (IMS-MS) method coupled to nanoelectrospray ionization (nESI-IMS-MS) has demonstrated significant advances for investigation of protein conformational states owing to its capability to retain solution structures upon transfer to the gas phase, also known as the "solution memory effect".[26−33] In addition, ions of the protein at high charge states or upon activation are associated with partially unfolding and/or extended structures, analogous to the unfolding processes induced by protonation in solution.[31,34] Furthermore, the integration of experimental ion mobilities (K) with theoretical calculations for candidate structures generated from molecular dynamics (MD) simulations has established IMS as a powerful structural probe.[27,28,30,33,35]

This report illustrates novelty and originality, as it provides gas-phase candidate structures from native-like to extended conformations as well as unfolding pathways for the histone H4.1 monomer. The findings of this study will provide the starting structure of the histone H4.1 monomer and information on the protein flexibility for the efficient discovery of specific inhibitors for the H4.1 monomer.

RESULTS AND DISCUSSION

nESI-TIMS-FAIMS-TOF MS. The MS spectra of H4.1 using native (65 mM NH_4Ac and 10 mM NH_4Ac) and denatured starting solutions (organic content) acquired using the nESI-TIMS-TOF MS configuration are shown in Figure 1a−c, respectively. The MS spectrum of native H4.1 exhibited a wide charge state distribution (CSD) spanning from charge state (z) 5+ to 17+ with a shift toward higher z as the NH_4Ac concentration was decreased. This suggests the solution memory effect during the transition from solution to the gas phase. The MS spectrum of denatured H4.1 showed an increase in the relative abundance of higher z and a noticeable decrease in the relative abundance of lower z, consistent with the exposure of basic residues due to molecular rearrangement in the high organic content of the starting solution condition.[32] A comparison of the MS distribution obtained using the tandem FAIMS-TIMS-MS configuration (Figures S1a and S2a) revealed a dependence on ion transmission when using the FAIMS stage, skewing the original charge state distribution.[21]

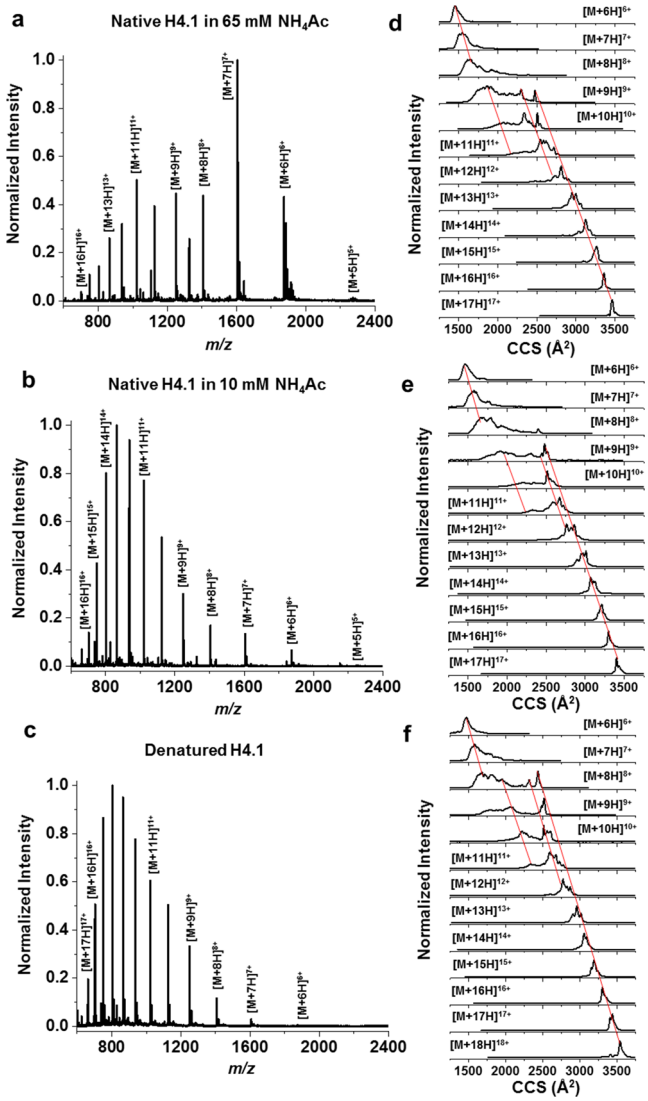

Figure 1. TIMS-MS mass spectra (a−c) and CCS profiles (d−f) of native H4.1 in 65 mM NH_4Ac, 10 mM NH_4Ac, and denatured H4.1, respectively. Data were acquired using "soft" TIMS ion injection settings with Sr_{TIMS} = 1.6 V/ms. The CCS profile of $[M + 5H]^{5+}$ is not shown due to a low signal. Note that CCS values increase with increasing charge states. The red lines mark a trend for C, P, and E conformations of H4.1.

The nESI-TIMS-TOF MS collision cross section (CCS) profiles of H4.1 in native (65 mM NH_4Ac and 10 mM NH_4Ac) and denatured starting solutions are shown in Figure 1d−f, respectively. These CCS profiles were acquired under soft ion

https://doi.org/10.1021/acsomega.1c03744
ACS Omega 2021, 6, 29567−29576

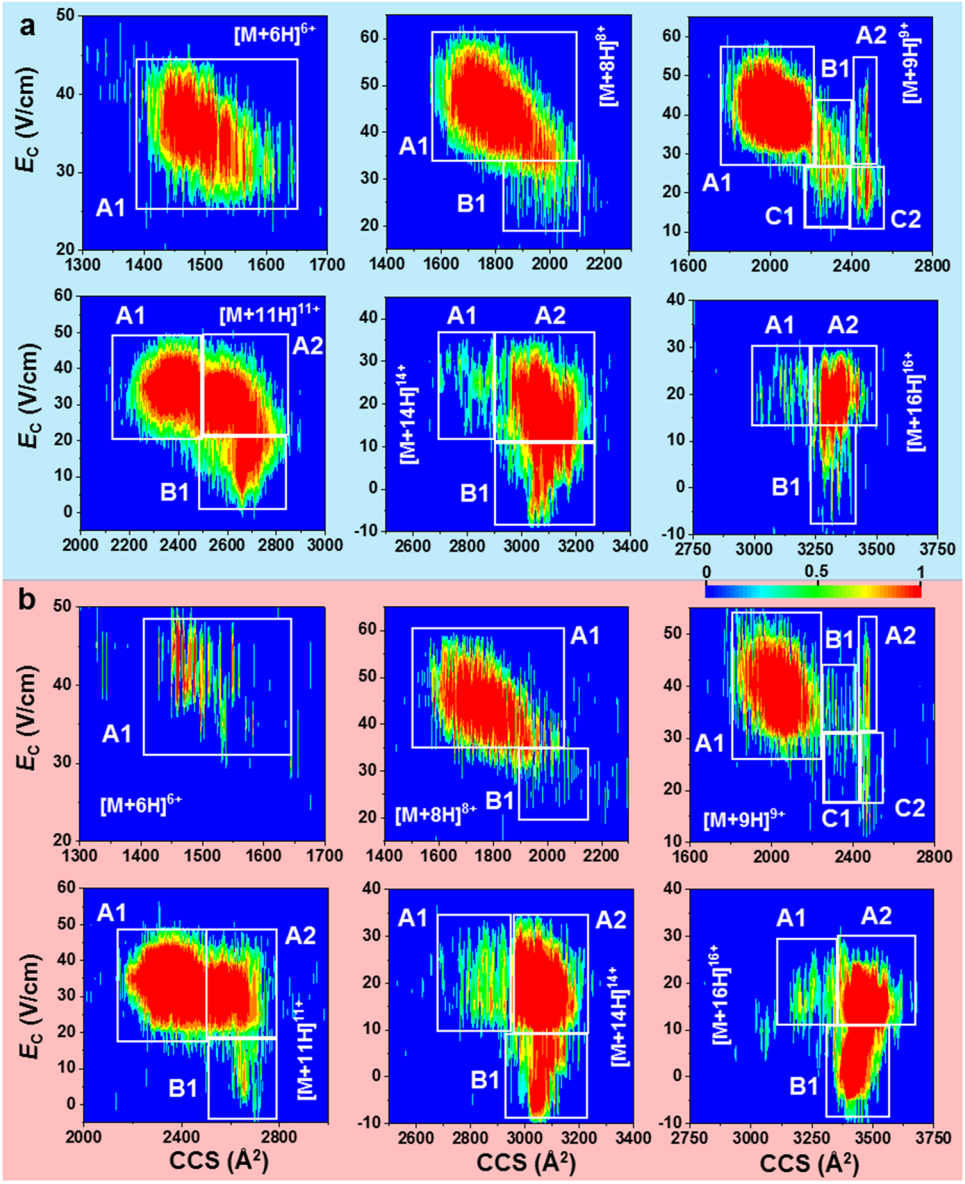

Figure 2. 2D FAIMS-TIMS palettes for selected charge states of H4.1 in native (10 mM NH_4Ac) and denatured starting buffer conditions. The 2D FAIMS-TIMS of all charge states is shown in the SI.

injection (ΔV_{TIMS} = 20 V). Inspection of these TIMS-MS CCS profiles revealed an increase in the CCS with the increase of charge states with multiple CCS bands observed per charge state in most of the intermediates and higher charge states. For example, the CCS profile of native H4.1 in 65 mM NH_4Ac showed that z = 6+ and 7+ exhibited a bell shape centered at ∼1470 and 1583 Å^2, respectively. These bands are likely characteristics of compact-like (C) conformations. The CCS profile of z = 8+ displayed a major band centered at ∼1679 Å^2 and minor bands at 1792, 1935, and 2395 Å^2, indicating the coexistence of C-like structures with a slightly less compact conformation. The CCS profiles of z = 9+ to 13+ display many CCS bands, consistent with coexisting ions populating C-like and partially unfolded (P-like) structures. The CCS profiles of z = 14+ to 17+ display a narrow CCS band with maxima at 3220, 3272, 3360, and 3470 Å^2, respectively. These characteristics imply that native H4.1 can adopt elongated (E-like) structures at higher charge states. When compared with the TIMS-MS CCS profiles of native H4.1 in 10 mM NH_4Ac, no differences were observed; however, considering better ion signal intensity observed in 10 mM NH_4Ac, this condition was used for native nESI-FAIMS-TIMS experiments. The TIMS-MS CCS profiles of denatured H4.1 (Figure 1f) showed some noticeable differences compared to those of native H4.1. For example, more CCS bands at ∼1682, 1720, 1815, 1952, 2210, 2316, and 2431 Å^2 were observed for z = 8+ of the denatured form (Table S1). Additionally, these CCS bands are more pronounced for denatured H4.1 compared to their native counterparts. These results further suggest "solution memory effects" on gas-phase structures of H4.1, evidenced not only by changes in CSD but also by mobility profiles.[21]

A comparison of CCS profiles for native (10 mM NH_4Ac) and denatured H4.1 acquired using nESI-TIMS-TOF MS (blue traces) and nESI-FAIMS-TIMS-TOF MS (red traces) configurations at soft ion injection (ΔV_{TIMS} = 20 V) is shown in Figures S1b and S2b. The FAIMS-TIMS-MS CCS profiles of the lowest (z = 6+ and 7+) and highest (z = 14+ to 17+) charge states were close to those obtained using the TIMS-MS

https://doi.org/10.1021/acsomega.1c03744
ACS Omega 2021, 6, 29567−29576

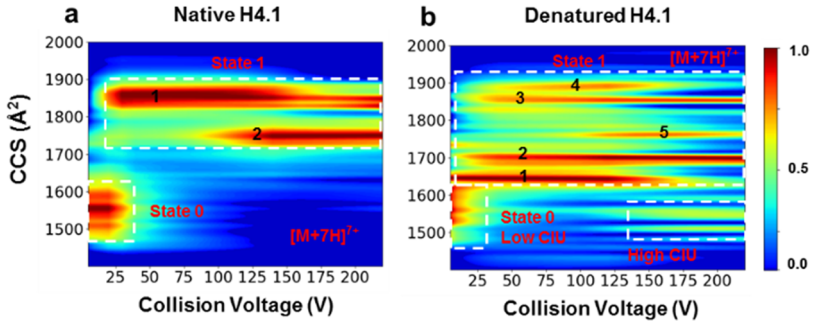

Figure 3. CIU-TIMS fingerprints for charge state 7+ of native H4.1 in 10 mM NH_4Ac (a) and denatured H4.1 (b).

configuration. The FAIMS-TIMS-MS CCS profiles of charge states 9+ to 13+ follow the established patterns of TIMS-MS CCS profiles with the coexistence of C- and P-like structures. A closer inspection revealed differences in the CCS profiles of data acquired using TIMS-MS and FAIMS-TIMS-MS configurations. That is, the addition of the FAIMS stage significantly affected the CCS profiles of the P-like structures (z = 8+ to 11+), consistent with our previous report.[21] For instance, in the case of z = 9+, the major CCS band was shifted to a higher CCS value in FAIMS-TIMS-MS (~2020 Å^2) compared to TIMS-MS (~1880 Å^2). A similar trend was observed for z = 8+, 10+, and 11+. These results implicate a subtle unfolding induced by ion heating in the FAIMS stage, consistent with previous reports.[22,36]

The compensation field profiles (E_C) of FAIMS-TOF MS (back traces) and FAIMS-TIMS-TOF MS (red traces) for H4.1 in native (10 mM NH_4Ac) and denatured starting solutions are shown in Figures S1c and S2c, respectively. No major difference in E_C profiles was observed between the data of native and denatured conditions, as well as with the inclusion of the TIMS separation. The total ion chromatogram (TIC) comprises ion signals ranging from -5 V/cm $\leq E_C \leq$ +55 V/cm, suggesting the existence of similar structures with varying dipole alignments. Overall, the E_C profiles of H4.1 exhibited higher E_C values for C-like structures (z = 6+ and 7+), while a decreasing trend toward $-E_C$ represents P-like and/or E-like structures. We noticed that a bimodal distribution with the lowest E_C values was observed for E-like structures, consistent with our previous report for histone H2A type 1 (H2A.1).[21]

To correlate features of CCS with E_C, the two-dimensional (2D) palettes of H4.1 were generated. Features in the 2D palette were defined using alphabets for high to low E_C and numbers for low to high CCS.[21] We noted that these features are charge state specific and correspond to different types of structures, which may or may not be separated based on mobility and m/z. The 2D palettes for typical charge states of native and denatured H4.1 are shown in Figure 2a,b, respectively. The 2D palettes of all charge states are displayed in Figures S1d and S2d. The 2D palettes of z = 6+ and 7+ for native and denatured H4.1 displayed homogeneous feature A1, corresponding to C-like structures. The 2D palettes of z = 8+ for both native and denatured H4.1 exhibited major feature A1 (CCS of ~1712 Å^2 and E_C of ~40 V/cm), a characteristic of a C-like structure. In addition, feature B1 (CCS of ~2290 Å^2 and E_C of ~27 V/cm) corresponding to a slightly less compact structure was observed at higher CCS and lower E_C ranges. The 2D palettes of z = 9+ for native and denatured H4.1 display multiple distinct features comprising features A1 (CCS of ~2020 Å^2 and E_C of ~40 V/cm), B1 (CCS of ~2200 Å^2 and E_C of ~33 V/cm), A2 (CCS of ~2470 Å^2 and E_C of ~40 V/cm), B1 (CCS of ~2200 Å^2 and E_C of ~20 V/cm), and B2 (CCS of ~2470 Å^2 and E_C of ~20 V/cm). These features are characteristic of C-like (feature A1), P-like (features B1 and A2), and E-like (features C1 and C2) structures. The 2D palettes of z = 10+ native and denatured H4.1 showed two features A1 (CCS of ~2280 Å^2 and E_C of ~38 V/cm) and A2 (CCS of ~2500 Å^2 and E_C of ~38 V/cm) at a higher E_C range, corresponding to P-like structures. In contrast, feature B1 (CCS of ~2500 Å^2 and E_C of ~15 V/cm) was observed at a lower E_C range, consistent with E-like structures due to more dipole alignments. The 2D palettes of z = 11+ of native and denatured H4.1 follow the established patterns of z = 10+. We noticed that features A2 and B1 of z = 10+ and 11+ were more abundant for the native form. For z = 12+ and 13+ of native and denatured H4.1, features A1, A2, and A3 have similar E_C values but significantly different CCS values, corresponding to P- and E-like structures. In addition, feature B1 was observed at a lower E_C range, corresponding to E-like structures with more dipole alignments. For $z \geq$ 14+, the 2D palettes of native and denatured H4.1 exhibited features A1 and A2 with slightly different CCS values in a higher E_C range, corresponding to the presence of multiple E-like structures. Moreover, feature B1 of these charge states exhibits higher relative abundance than that of the lower charge states, consistent with more dipole alignments.

Collision-Induced Unfolding of H4.1. Our TIMS-MS and FAIMS-TIMS-MS results revealed that H4.1 adopts heterogeneous structures. To further characterize the gas-phase structural features of H4.1, we utilized collision-induced unfolding (CIU) to probe the conformational change as a function of activation voltage. The CIU fingerprints for charge state 7+ of native and denatured H4.1 are shown in Figure 3. The CIU fingerprints of all charge states are displayed in Figure S3.

The inspection of H4.1 CIU fingerprints revealed a significant impact of the native (10 mM NH4Ac) and denatured starting solutions on the gas-phase H4.1 structures. The major differences were observed for the lowest charge state. For example, the CIU fingerprint of z = 7+ (Figure 3) for both native and denatured H4.1 exhibited ions populating C- and P-like structures; however, their CIU pathways were dependent on the starting solution conditions. A closer inspection of the fingerprint for native H4.1 (Figure 3a) revealed that at the lowest collision voltage (~5–30 V), the CCS was centered at ~1580 Å^2 (state 0), corresponding to C-like structures. As the collision voltage was increased (~25–130 V), the CCS dramatically increased to ~1870 Å^2

https://doi.org/10.1021/acsomega.1c03744
ACS Omega 2021, 6, 29567−29576

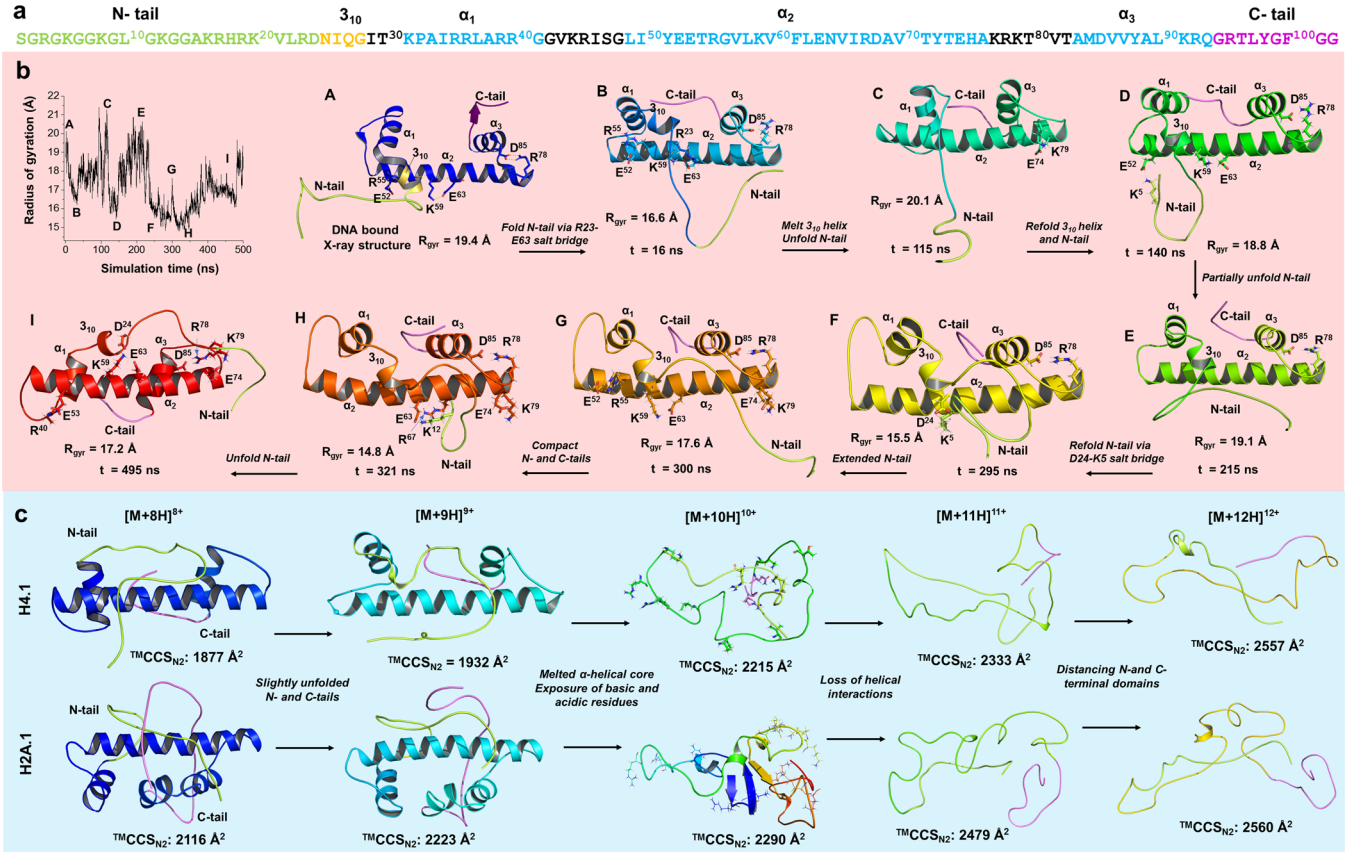

Figure 4. Molecular modeling. (a) Amino acid sequence of H4.1. Residues corresponding to α- and 3_{10}-helices and the N- and C-terminal regions are marked. (b) Radius of gyration as a function of CMD simulation time. The snapshots of the solution phase of H4.1 are labeled from A to I. Residues corresponding to salt bridges are indicated. (c) Comparison of the gas-phase unfolding pathways between H4.1 and H2A.1.

(conformation 1 of state 1), consistent with P-like structures. These results are consistent with collision-induced unfolding.[37] Interestingly, at higher collision voltages (~125 to 220 V), the CCS decreased to ~1750 Å^2 (conformation 2 of state 1), implying the refolding of H4.1 toward a more compact conformation. Typically, gas-phase activation results in unfolding;[37] however, compaction of protein structures upon activation has been reported.[21,38,39] This is particularly relevant since H4.1 has an intrinsically disordered N-terminal tail, which may or may not be exposed during the gas-phase unfolding transient. We noticed that a low abundance of conformation 1 (CCS of ~1870 Å^2) remained at the highest collision voltages (~160 to 220 V), suggesting the coexistence of conformations 1 and 2.

A closer inspection of the CIU fingerprint for denatured H4.1 (Figure 3b) showed that at the lowest collision voltage (~5 to 25 V), the CCS value was observed at ~1580 Å^2 (state 0 at low CIU), corresponding to C-like structures. When the collision voltage was increased from 10 to 120 V, the CCS increased to ~1650 Å^2 (conformation 1 of state 1), consistent with P-like structures. As the collision voltage was further increased from 25 to 220 V, the CCS increased to ~1690 Å^2 (conformation 2 of state 1). In addition, conformation 3 with higher CCS (~1870 Å^2) coexisted in the same voltage range. When the collision voltage was increased from 50 to 125 V, the CCS further increased to ~1910 Å^2 (conformation 4 of state 1). Interestingly, by further increasing the collision voltage from 125 to 200 V, the CCS decreased to ~1790 Å^2 (conformation 5 of state 1), consistent with more compact structures. At the highest collision voltage (~150 to 220 V), the CCS further decreased to ~1580 Å^2 (state 0 at high CIU), corresponding to C-like structures. These results suggest that while the denatured starting solution maintained H4.1 compact structures, it also induced intramolecular arrangements to differentiate the CIU patterns of native and denatured H4.1. In the case of z = 8+, the CIU fingerprints of native and denatured showed mainly three CIU states: 0 for C-like, 1 for P-like, and 2 for E-like structures. In addition, no difference was observed for the CIU fingerprints for native and denatured H4.1 at higher charge states (z = 9+ to 17+).

CMD Simulations of Solution-Phase H4.1. Figure 4a shows the amino acid sequence, α-helices, 3_{10}-helices, and the N- and C-terminal regions of H4.1. The radius of gyration (R_{gyr}) profile along the simulation time was utilized for the analysis of H4.1 structural rearrangement in solution. For example, the snapshots (A–I) of H4.1 conformations are shown in Figure 4b. The initial DNA-bound X-ray structure of H4.1 (A) comprises three α-helices (α1 to α3), one 3_{10}-helix, and an intrinsically disordered N-terminal tail. A close inspection of conformation A revealed that H4.1 structural elements are stabilized in the nucleosome by hydrogen bonding to DNA and by interactions with α-helices from histones H3.[2] In addition, the N-terminal tail of the DNA-bound H4.1 structure was highly extended, leading to an extended conformation with a calculated R_{gyr} of 19.4 Å. At 16 ns, the N-terminal tail was partially folded via formation of the R23–E63 salt bridge (conformation B). At 115 ns, the N-terminal vicinity was collapsed due to melting of the 3_{10}-helix

https://doi.org/10.1021/acsomega.1c03744
ACS Omega 2021, 6, 29567–29576

and the rearrangement of α3 on the C-terminus, leading to formation of conformation C (R_{gyr} = 20.1 Å). At 140 ns, the 3_{10}-helix was gradually refolded, and the N- and C-terminal tails were folded, resulting in conformation D (R_{gyr} = 18.8 Å), stabilized by salt bridges K^5/E^{52}, K^{59}/E^{63}, and D^{85}/R^{78}. At 215 ns, the N-terminal tail was partially unfolded, while the C-tail was folded, leading to conformation E (R_{gyr} = 19.1 Å). Up to 295 ns, both the N- and C-terminal tails were folded, leading to conformation F with a R_{gyr} of 15.5 Å, stabilized by salt bridges K^5/D^{24} and R^{78}/D^{85}. At 320 ns, the N-terminal tail was unfolded, leading to partially unfolded conformation G (R_{gyr} = 17.6 Å) stabilized by salt bridges R^{55}/E^{52}, R^{59}/E^{63}, K^{79}/E^{74}, and R^{78}/D^{85}. At 321 ns, both the N- and C-terminal tails were folded, leading to compact conformation H with the smallest R_{gyr} of 14.8 Å, stabilized by salt bridges R^{67}/E^{63}, K^{12}/E^{63}, R^{78}/D^{85}, and K^{79}/E^{74}. Interestingly, the α2-helix was slightly bent near the N-terminal vicinity (H, Figure 4b). Further simulations (e.g., t = 495 ns) lead to conformation I with a larger R_{gyr} of 17.2 Å due to unfolded N-terminal tail. The effects of water box thickness and nonbonded cutoff are shown in Figure S5 and described in the Supporting Information.

Comparison of Gas-Phase Structural Features between H2A.1 and H4.1. Figure 4c shows the representative gas-phase candidate structures for the main CCS features of H4.1 observed from TIMS-MS experiments (all candidate structures for 6+ to 18+ are shown in Figure S4 and summarized in Table S1). For the most compact structures (6+ to 9+), two trends were observed: (i) a gas-phase compact structure where the α2-helix was gradually bent and partially melted and (ii) a gas-phase compact structure that preserves the α2-helix structure from that of the native solution (conformation H). A closer inspection revealed that the major structural changes in H4.1 were associated with the unfolding of N- and C-terminal tails, disruption of inter-α-helical interactions, leading to exposed charge residues, increasing the distance of N- and C-terminal domains, and extending the N- and C-terminal tails in higher charge states. For example, the candidate for z = 8+ exhibited a C-like structure with a calculated CCS_{N2} value of 1877 $Å^2$. A comparison of the unfolding pathways between H4.1 and H2A.1[21] illustrated a potential unfolding pathway for H4.1 as a function of charge state and CCS ranges. The candidate structures of both H4.1 and H2A.1 in the C-like conformation have the N- and C-terminal tails tightly folded toward the α-helical core. The candidate for z = 9+ of H4.1 displayed a subtle rearrangement in both N- and C-terminal domains, leading to a refolding of the 3_{10}-helix in the N-terminal vicinity and a slightly unfolding of the C-terminal tail, consistent with the structural rearrangement of the candidate for z = 9+ of H2A.1. Overall, these results demonstrate that the C-like structure of H4.1 exhibits a similar folding motif as observed for H2A.1. That is, both N- and C-terminal domains were folded toward the α-helical core. The candidate structure of z = 10+ displays a major structural rearrangement associated with melting of α-helices, leading to the destabilization of the secondary structure and exposed basic and acidic residues K^8, R^{19}, K^{31}, R^{35}, R^{39}, K^{59}, R^{67}, K^{91}, R^{92}, R^{95}, and E^{74}, consistent with the unfolding of H2A.1. Inspection of candidate structures of z = 11+ to 18+ (Figures 4c and S4) revealed that H4.1 adopted E-like structures with the high content of the random coil, in agreement with our experimental results. For example, most of the helical interactions in the candidate structure of z = 11+ were loose, followed by the distance between the N- and C-terminal domains. Moreover, the candidate structures of z = 12+ and 13+ exhibit a further expansion between the N- and C-terminal domains, leading to a highly extended conformation. Furthermore, the structures of z = 13+ and 14+ display a rearrangement of the N- and C-terminal domains, promoting an E-like conformation. For $z \geq$ 15+, the candidates exhibit highly random coil structures with an extended C-terminus.

Influence of the Charge Distribution on the Dipole Alignment of H4.1. The 2D FAIMS-TIMS palettes present a correlation between dipole alignment, CCS, and the charge state distribution. The effect of charge on the dipole alignment is illustrated by charge state 17+ of denatured H4.1. As shown in Figure 5a, the candidate structures representative for

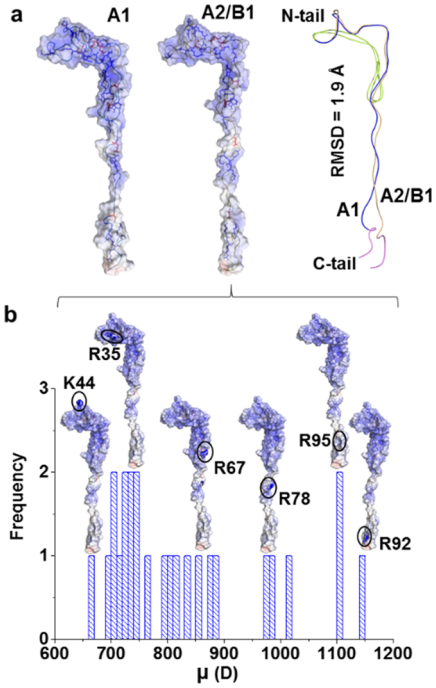

Figure 5. (a) Candidate structures for z = 17+ of H4.1. (b) Frequency plot of dipole moment values (μ) for all 25 structures with different charge distributions for z = 17+ based on the candidate structure of A2/B. The neutralized basic residue (R or K) is marked by a black circle.

features A1 (CCS of ~3402 $Å^2$) and A2/B1 (CCS of ~3442 $Å^2$) adopt an E-like conformation with a relatively narrow CCS distribution. In addition, these candidates have high structural similarity, evidenced by a small backbone RMSD of ~1.9 Å. Moreover, most basic residues (blue sticks) and all basic residues (red sticks) are solvent exposed. All dipole moment values (Table S2) for the candidate structure of feature A2/B1 were calculated in YASARA using the AMBER03 force field. A total of seven acidic residues (D^{24}, E^{52}, E^{53}, E^{63}, D^{68}, E^{74}, and D^{85}) were deprotonated, while 24 of 25 basic residues (R^3, K^5, K^8, K^{12}, K^{16}, R^{17}, R^{19}, K^{20}, R^{23}, K^{31}, R^{35}, R^{36}, R^{39}, R^{40}, K^{44}, R^{45}, R^{55}, K^{59}, R^{67}, K^{77}, R^{78}, K^{79}, K^{91}, R^{92}, and R^{95}) were protonated, and the last basic residue was neutralized, leading to a combination of 25 structures having different charge distributions. The charge distribution dependence on the dipole is shown in Figure 5b. A closer inspection revealed that the largest dipole moment value of 1149 D was observed for a structure with neutralized residue R^{92} near the C-terminus,

https://doi.org/10.1021/acsomega.1c03744
ACS Omega 2021, 6, 29567−29576

whereas the smallest dipole moment value of 664 D was observed for a structure with neutralized residue K[44] at the N-terminus. While we cannot exclude other potential candidate structures with similar CCS values, this example demonstrates that the charge distribution, particularly in structures having exposed acidic and basic residues, can lead to a wide distribution of the dipole alignment. These results are in good agreement with the previous report that suggested dipole alignment under FAIMS experiments for molecular ions having dipole values above 300 D.[40]

CONCLUSIONS

In this work, DNA-free H4.1 structures have been addressed using FAIMS-TIMS-MS in parallel with MD simulations.

The TIMS-TOF MS experiments under soft ion injection conditions showed that H4.1 adopts different structures ranging from C-like to P-like and subsequently to E-like conformations. The FAIMS-TIMS-MS results showed that native-like structures were retained throughout the FAIMS stage for the lowest charge states (6+ and 7+). However, P-like structures (z = 9+ to 11+) were sensitive to ion heating in the FAIMS stage. Moreover, no change in the CCS profiles were observed for the highest charge states by the addition of the FAIMS stage, allowing the assessment of the influence of the conformational diversity and charge distribution on the dipole alignment at high electric fields. The results from CIU experiments revealed heterogeneous structures for H4.1. Interestingly, "refolding after unfolding" upon activation was observed for the lowest charge state (z = 7+). The MD simulations revealed the native conformation of H4.1 with both N- and C-terminal domains folded toward the α-helical core. The gas-phase unfolding pathways showed that H4.1 exhibited major structural rearrangements associated with unfolding of the N- and C-terminal vicinities and disruption of inter-α-helical interactions, leading to the exposure of charge residues and increasing the distance of N- and C-terminal domains in higher charge states.

Complementary CCS and dipole calculations illustrated that charge distributions in an E-like structure, where basic and acidic residues are exposed (e.g., z = 17+), are sufficient to induce differences in the dipole alignment at high electric fields, particularly when their CCS profiles exhibit a narrow band distribution.

In conclusion, the data offer important insights into DNA-free H4.1 structures and differences when compared with H2A.1. These data can be further used as guidelines for structure-based drug design specifically for histones.

EXPERIMENTAL SECTION

Materials and Reagents. Recombinant human histone H4.1 (accession number: P62805) was purchased from EpiCypher (Durham, NC). All solvents used in this study were of analytical grade or better and purchased from Fisher Scientific (Pittsburgh, PA). Low-concentration Tuning Mix standard (G1969-85000) was purchased from Agilent Technologies (Santa Clara, CA) and used as received. Stock H4.1 was prepared in ultrapure water and extensively dialyzed against 10 mM ammonium acetate (NH_4Ac) buffer for ~36 h by changing buffer every ~12 h. Native H4.1 samples were prepared by diluting histone stock to 10 μM in 10 and 65 mM NH_4Ac solutions, whereas the denatured H4.1 sample was prepared at 10 μM in a methanol/water/formic acid (v/v 50:49:1) solution.

nESI-FAIMS-TIMS-TOF MS Instrument. Details regarding the operation of the nanoelectrospray ionization (nESI)-FAIMS-TIMS-TOF MS instrument can be found elsewhere.[21] Briefly, the system comprised a "dome" FAIMS unit with a 2 mm annular gap (g)[41−43] orthogonally mounted to a custom-built TIMS-TOF MS (Bruker Daltonics Inc., MA).[44] The FAIMS system was controlled by a custom driver outputting a bisinusoidal waveform with a frequency of 1 MHz and an amplitude (dispersion voltage, DV) of 4 kV in the negative polarity mode applied to the inner electrode (GAA Custom Electronics, LLC). The compensation voltage (CV) was linearly scanned with a rate (Sr_{FAIMS}) of 1.0 V/min and expressed in the compensation field (E_C) by the equation E_C = CV/g.

A nESI emitter was made from a quartz capillary (o.d. = 1.0 mm) using a P2000 laser puller (Sutter Instruments Co., Novato, CA). The voltages for the nESI emitter and the curtain plate were set at 2.4 and 1.0 kV, respectively. N_2 gas was purified by a GC filter (Agilent, RMSN-4) and used to carry ions into the dome FAIMS. The carrier gas flow was controlled at 2 L/min by a digital flowmeter (MKS Instruments).

In TIMS, nitrogen (N_2) was used as a buffer gas at a constant velocity controlled by the pressure difference between the funnel entrance (P_1 = 2.6 mbar) and exit (P_2 = 1.1 mbar) at ca. 300 K.[44] A radio frequency (rf) voltage of 250 Vpp at a frequency of 880 kHz was applied to TIMS electrodes. The reduced mobility (K_0) of ions depended on the gas flow velocity (v_g), elution voltage (V_e), base voltage (V_{out}), and ramp time (t_{ramp}) and can be expressed by eq 1

$$K_0 = \frac{v_g}{E} \cong \frac{A}{V_e - V_{out}} \quad (1)$$

where A is a calibration constant determined using the known mobility of Tuning Mix ions m/z 622.029 ($1/K_0$ = 0.985 Vs/cm^2), 922.009 ($1/K_0$ = 1.190 Vs/cm^2), 1221.991 ($1/K_0$ = 1.382 Vs/cm^2), and 1821.952 ($1/K_0$ = 1.729 Vs/cm^2).[25,45] The K_0 of an ion is correlated to the collision cross section (CCS, Ω) via the Mason−Schamp equation (eq 2)[46]

$$\Omega = \frac{(18\pi)^{1/2}}{16}\frac{z}{(k_B T)^{1/2}}\left[\frac{1}{m_I} + \frac{1}{m_b}\right]^{1/2}\frac{1}{K_0}\frac{1}{N^*} \quad (2)$$

where z is the charge of the ion, kB is the Boltzmann constant, T is the temperature, N^* is the bath gas number density, and m_I and m_b are the masses of the molecular ion and the bath gas, respectively.[25,45]

To avoid potential ion activation prior to mobility analysis, all experiments were carried out using soft ion transmission and trapping conditions.[47,48] A voltage difference (ΔV) between 10 to 20 V was maintained between the deflector (V_{def}) and the funnel entrance (V_{fun}), as well as between the funnel entrance and the TIMS analyzer (V_{ramp}). A V_{def} of −140V, a V_{fun} of −160 V, a base voltage (V_{out}) of 60V, and a V_{ramp} of −180 to −20 V were used for all measurements. The TIMS scan rate (Sr_{TIMS}) was set at 1.6 V/ms.

The reference FAIMS-TOF MS spectra were collected on the TIMS transmission mode (without trapping), while the reference TIMS-TOF MS spectra were collected with the FAIMS unit detached. The 4D FAIMS-TIMS-TOF MS data were acquired by summing the TIMS-MS spectra (~100

https://doi.org/10.1021/acsomega.1c03744
ACS Omega 2021, 6, 29567−29576

spectra) every 0.9 V/cm over the E_C = −15−75 V/cm range. Data were processed using Data Analysis 5.0 (Bruker Daltonics Inc., Billerica, MA) and Microcal Origin 7.0. (OriginLab, Northampton, MA).

The CIU experiments were performed by varying V_{def} with a 20 V interval. Voltages V_{fun} and V_{ramp} were changed relative to V_{def} to ensure a homogeneous axial electric field in all CIU experiments.[49] The CIU data were analyzed using CIU Suite 2 software.[50]

Classical Molecular Dynamics (CMD) Simulations. CMD simulations were carried out as previously described.[21,51] Hydrogen atoms were added to the initial X-ray structure of H4.1 (chain B, PDB entry: 1KX5)[2] and the hydrogen network in the protein was optimized at the pH 7.0 condition. The protein system was subsequently solvated using the VMD package[52] with a TIP3P water box cutoff of 10 Å. The solvated system was neutralized by adding 150 mM NaCl randomly into the bulk water using autoionize plugin in VMD. All-atom simulations were performed in an explicit solvent at 310 K using NAMD 2.14 (NVIDIA CUDA acceleration)[53] with the modified CHARMM36 (CHARMM36m) force field for intrinsically disordered proteins.[54] Long-range interactions were treated with the particle mesh Ewald method with a 12 Å nonbonded cutoff.[55] To clarify the effects of water box thickness and nonbonded cutoff, CMD simulations of a system using a water box cutoff of 25 Å and a nonbonded cutoff of 8 Å were performed. The system was energy minimized for 500 000 steps using the conjugate gradient and the line search algorithm, followed by heating at 1 K/ps from 0 to 310 K. After reaching 310 K, a 100 ps equilibration run with an integration time step of 1 fs in the NVT ensemble was performed using Langevin dynamics to maintain the temperature at 310 K. The production run of 500 ns was performed in the NPT ensemble at 1 atm and 310 K with Langevin coupling and an integration time step of 2 fs. Trajectory files were saved every 0.1 ns for analysis.

Simulated Annealing Molecular Dynamics (SAMD) Simulations. SAMD simulations were used to generate gas-phase structures.[21,28,56] The smallest radius of gyration (R_{gyr} = 14.8 Å) structure obtained from the CMD (conformation H, Figure 4b) was used as the starting structure. To ensure oversampling of total conformation spaces, SAMD simulations were performed for 220 cycles with the temperature ramping between T1 (300 K) and T2 (800 K): 50 ps relaxation at T1, 5 ps heating to T2, 50 ps relaxation at T2, and 2 ps cooling to T1, 5 ps minimization, and a 20 K increase between T1 and T2. An NVT ensemble with an integration time step of 2 fs was used. While this method generated most of the candidates (extended compact 7+ to unfolded 18+), the compact structures for 6+ to 9+ were obtained using a supervised NVT ensemble with boundary restrains to force the conversion into more compact structures followed by energy minimization.

Steered Molecular Dynamics (SMD) Simulations. Details regarding the gas-phase SMD simulations can be found elsewhere.[21,57] The extended unfolding structures of H4.1 were generated by pulling the center of mass of the α-carbons of residue S at position 1 (S^1) on the N-terminus at a rate of 0.25 Å/ns for 100 ns while anchoring residue G at position 102 (G^{102}) on the C-terminus. The production run was performed in the NVT ensemble with an integration time step of 2 fs. The trajectory structures were saved at every 0.5 ps for further analysis. The reproducibility and reliability of SMD simulations were also clarified.

Theoretical CCS Calculation and Cluster Analysis. The theoretical CCS values of H4.1 in N_2 gas (CCS_{N2}) were calculated using the trajectory method (TM) integrated with IMoS v.1.10b software.[58−61] The candidate structures of H4.1 are classified based on the comparison of root-mean-square deviation (RMSD) for all structures and classified into clusters.[28,62] The statistical processing codes[62] written in R (https://www.r-project.org) were used in this work. When candidates from the cluster families were determined, charge assignment was performed by scoring the relative solvent accessibility (RSA) of basic and acidic residues in H4.1.[63] The dipole moments of individual candidates were computed with the AMBER03 force field using YASARA software (www.yasara.org). The electric dipole moment p in the unit of C·m is the length of vector P, which is defined by eq 3

$$\vec{P} = \sum_i q_i^*(\vec{R}_i - \vec{C}) \quad (3)$$

In this formula, q is the charge of atom i, R is its Cartesian coordinate, and C is the geometric center. Finally, all of the structural models were displayed using PyMOL (Schrodinger, Inc.).

■ ASSOCIATED CONTENT

Supporting Information

The Supporting Information is available free of charge at https://pubs.acs.org/doi/10.1021/acsomega.1c03744.

Complete FAIMS-TIMS analyses of native and denatured H4.1. CIU-TIMS fingerprints of all charge states; candidate structures of all charge states; table of all experimental and theoretical CCS values and a table of dipole values; and structural coordinates for in-solution and gas-phase candidate structures of H4.1 (PDF)

■ AUTHOR INFORMATION

Corresponding Author

Francisco Fernandez-Lima − *Department of Chemistry and Biochemistry, Florida International University, Miami, Florida 33199, United States; Biomolecular Science Institute, Florida International University, Miami, Florida 33199, United States;* orcid.org/0000-0002-1283-4390; Email: fernandf@fiu.edu

Author

Khoa N. Pham − *Department of Chemistry and Biochemistry, Florida International University, Miami, Florida 33199, United States;* orcid.org/0000-0001-7449-1226

Complete contact information is available at: https://pubs.acs.org/10.1021/acsomega.1c03744

Notes

The authors declare no competing financial interest.

■ ACKNOWLEDGMENTS

This work was supported by the NIH 1R01GM134247-01 grant to FFL. The authors would like to thank Dr. Prem Chapagain for discussions of the theoretical modeling, Dr. Alexander Shvartsburg for the integration of the "dome" FAIMS stage, and Dr. Mark E. Ridgeway and Dr. Melvin A. Park for the discussions on the FAIMS-TIMS-MS interface and

data processing. We also thank Dr. Brandon Ruotolo and his team for the integration of CIU-TIMS data into the CIU suite.

REFERENCES

(1) Hansen, J. C.; Lu, X.; Ross, E. D.; Woody, R. W. Intrinsic Protein Disorder, Amino Acid Composition, And Histone Terminal Domains. *J. Biol. Chem.* **2006**, *281*, 1853−1856.
(2) Davey, C. A.; Sargent, D. F.; Luger, K.; Maeder, A. W.; Richmond, T. J. Solvent Mediated Interactions In The Structure Of The Nucleosome Core Particle At 1.9 A Resolution. *J. Mol. Biol.* **2002**, *319*, 1097−1113.
(3) Bowman, G. D.; Poirier, M. G. Post-Translational Modifications Of Histones That Influence Nucleosome Dynamics. *Chem. Rev.* **2015**, *115*, 2274−2295.
(4) McGinty, R. K.; Tan, S. Nucleosome Structure And Function. *Chem. Rev.* **2015**, *115*, 2255−2273.
(5) Jenuwein, T.; Allis, C. D. Translating The Histone Code. *Science* **2001**, *293*, 1074−1080.
(6) Kurdistani, S. K. Histone Modifications As Markers Of Cancer Prognosis: A Cellular View. *Br. J. Cancer* **2007**, *97*, 1−5.
(7) Wolffe, A. P. Histone Deacetylase: A Regulator Of Transcription. *Science* **1996**, *272*, 371−372.
(8) van Attikum, H.; Gasser, S. M. The Histone Code At DNA Breaks: A Guide To Repair? *Nat. Rev. Mol. Cell Biol.* **2005**, *6*, 757−765.
(9) Seligson, D. B.; Horvath, S.; Shi, T.; Yu, H.; Tze, S.; Grunstein, M.; Kurdistani, S. K. Global Histone Modification Patterns Predict Risk Of Prostate Cancer Recurrence. *Nature* **2005**, *435*, 1262−1266.
(10) Keck, K. M.; Pemberton, L. F. Histone Chaperones Link Histone Nuclear Import And Chromatin Assembly. *Biochim. Biophys. Acta, Gene Regul. Mech.* **2012**, *1819*, 277−289.
(11) Silk, E.; Zhao, H.; Weng, H.; Ma, D. The Role Of Extracellular Histone In Organ Injury. *Cell Death Dis.* **2017**, *8*, No. e2812.
(12) Meara, C. H. O.; et al. Neutralizing The Pathological Effects Of Extracellular Histones With Small Polyanions. *Nat. Commun.* **2020**, *11*, No. 6408.
(13) Abrams, S. T.; et al. Circulating Histones Are Mediators Of Trauma-Associated Lung Injury. *Am. J. Respir. Crit. Care Med.* **2013**, *187*, 160−169.
(14) Allam, R.; et al. Histones From Dying Renal Cells Aggravate Kidney Injury Via TlR2 And TlR4. *J. Am. Soc. Nephrol.* **2012**, *23*, 1375−1388.
(15) Zuo, Y.; et al. Neutrophil Extracellular Traps In COVID-19. *JCI Insight* **2020**, *5*, No. e138999.
(16) Silvestre-Roig, C.; et al. Externalized Histone H4 Orchestrates Chronic Inflammation By Inducing Lytic Cell Death. *Nature* **2019**, *569*, 236−240.
(17) Fuchs, T. A.; Bhandari, A. A.; Wagner, D. D. Histones Induce Rapid And Profound Thrombocytopenia In Mice. *Blood* **2011**, *118*, 3708−3714.
(18) Wichapong, K.; Silvestre-Roig, C.; Braster, Q.; Schumski, A.; Soehnlein, O.; Nicolaes, G. A. F. Structure-Based Peptide Design Targeting Intrinsically Disordered Proteins: Novel Histone H4 And H2A Peptidic Inhibitors. *Comput. Struct. Biotechnol. J.* **2021**, *19*, 934−948.
(19) Macalino, S. J. Y.; Basith, S.; Clavio, N. A. B.; Chang, H.; Kang, S.; Choi, S. Evolution Of In Silico Strategies For Protein-Protein Interaction Drug Discovery. *Molecules* **2018**, *23*, 1963.
(20) Feixas, F.; Lindert, S.; Sinko, W.; McCammon, J. A. Exploring The Role of Receptor Flexibility In Structure-Based Drug Discovery. *Biophys. Chem.* **2014**, *186*, 31−45.
(21) Pham, K. N.; Mamun, Y.; Fernandez-Lima, F. Structural Heterogeneity of Human Histone H2A.1. *J. Phys. Chem. B* **2021**, *125*, 4977−4986.
(22) Shvartsburg, A. A.; Bryskiewicz, T.; Purves, R. W.; Tang, K.; Guevremont, R.; Smith, R. D. Field Asymmetric Waveform Ion Mobility Spectrometry Studies Of Proteins: Dipole Alignment In Ion Mobility Spectrometry? *J. Phys. Chem. B* **2006**, *110*, 21966−21980.
(23) Shvartsburg, A. A.; Smith, R. D. High-Resolution Differential Ion Mobility Spectrometry Of A Protein. *Anal. Chem.* **2013**, *85*, 10−13.
(24) Revercomb, H. E.; Mason, E. A. Theory of Plasma Chromatography/Gaseous Electrophoresis. *Anal. Chem.* **1975**, *47*, 970−983.
(25) Gabelica, V.; et al. Recommendations For Reporting Ion Mobility Mass Spectrometry Measurements. *Mass Spectrom. Rev.* **2019**, *38*, 291−320.
(26) Clemmer, D. E.; Jarrold, M. F. Ion Mobility Measurements And Their Applications To Clusters and Biomolecules. *J. Mass Spectrom.* **1997**, *32*, 577−592.
(27) Ruotolo, B. T.; Benesch, J. L.; Sandercock, A. M.; Hyung, S. J.; Robinson, C. V. Ion Mobility-Mass Spectrometry Analysis Of Large Protein Complexes. *Nat. Protoc.* **2008**, *3*, 1139−1152.
(28) Fernandez-Lima, F. A.; Wei, H.; Gao, Y. Q.; Russell, D. H. On The Structure Elucidation Using Ion Mobility Spectrometry And Molecular Dynamics. *J. Phys. Chem. A* **2009**, *113*, 8221−8234.
(29) Jurneczko, E.; Barran, P. E. How Useful Is Ion Mobility Mass Spectrometry for Structural Biology? The Relationship Between Protein Crystal Structures And Their Collision Cross Sections In The Gas Phase. *Analyst* **2011**, *136*, 20−28.
(30) Landreh, M.; et al. Integrating Mass Spectrometry with MD Simulations Reveals The Role Of Lipids In Na+/H+ Antiporters. *Nat. Commun.* **2017**, *8*, No. 13993.
(31) Pagel, K.; Natan, E.; Hall, Z.; Fersht, A. R.; Robinson, C. V. Intrinsically Disordered P53 and Its Complexes Populate Compact Conformations In The Gas Phase. *Angew. Chem., Int. Ed.* **2013**, *52*, 361−365.
(32) Jeanne Dit Fouque, K.; Moreno, J.; Fernandez-Lima, F. Exploring The Conformational Space Of Growth-Hormone-Releasing Hormone Analogues Using Dopant Assisted Trapped Ion Mobility Spectrometry−Mass Spectrometry. *J. Phys Chem. B* **2019**, *123*, 6169−6177.
(33) Wyttenbach, T.; Bowers, M. T. Structural Stability From Solution To The Gas Phase: Native Solution Structure of Ubiquitin Survives Analysis In A Solvent-Free Ion Mobility−Mass Spectrometry Environment. *J. Phys. Chem. B* **2011**, *115*, 12266−12275.
(34) Shi, H.; Pierson, N. A.; Valentine, S. J.; Clemmer, D. E. Conformation Types Of Ubiquitin $[M+8h]^{8+}$ Ions From Water:-Methanol Solutions: Evidence For The N And A States In Aqueous Solution. *J Phys. Chem. B* **2012**, *116*, 3344−3352.
(35) Koeniger, S. L.; Merenbloom, S. I.; Clemmer, D. E. Evidence For Many Resolvable Structures Within Conformation Types Of Electrosprayed Ubiquitin Ions. *J. Phys. Chem. B* **2006**, *110*, 7017−7021.
(36) Shvartsburg, A. A.; Li, F.; Tang, K.; Smith, R. D. Distortion Of Ion Structures By Field Asymmetric Waveform Ion Mobility Spectrometry. *Anal. Chem.* **2007**, *79*, 1523−1528.
(37) Benesch, J. L. P. Collisional Activation of Protein Complexes: Picking Up The Pieces. *J. Am. Soc. Mass Spectrom.* **2009**, *20*, 341−348.
(38) Hall, Z.; Politis, A.; Bush, M. F.; Smith, L. J.; Robinson, C. V. Charge-State Dependent Compaction And Dissociation Of Protein Complexes: Insights From Ion Mobility And Molecular Dynamics. *J. Am. Chem. Soc.* **2012**, *134*, 3429−3438.
(39) Zhou, M.; Liu, W.; Shaw, J. B. Charge Movement And Structural Changes In The Gas-Phase Unfolding Of Multimeric Protein Complexes Captured By Native Top-Down Mass Spectrometry. *Anal. Chem.* **2020**, *92*, 1788−1795.
(40) Shvartsburg, A. A.; Noskov, S. Y.; Purves, R. W.; Smith, R. D. Pendular Proteins In Gases And New Avenues For Characterization Of Macromolecules By Ion Mobility Spectrometry. *Proc. Natl. Aca. Sci. U.S.A.* **2009**, *106*, 6495−6500.
(41) Guevremont, R.; Purves, R. W. Atmospheric Pressure Ion Focusing In A High-Field Asymmetric Waveform Ion Mobility Spectrometer. *Rev. Sci. Instrum.* **1999**, *70*, 1370−1383.
(42) Guevremont, R.; Barnett, D. A.; Purves, R. W.; Vandermey, J. Analysis Of A Tryptic Digest Of Pig Hemoglobin Using Esi-FAIMS-MS. *Anal. Chem.* **2000**, *72*, 4577−4584.

https://doi.org/10.1021/acsomega.1c03744
ACS Omega 2021, 6, 29567−29576

(43) Guevremont, R. High-Field Asymmetric Waveform Ion Mobility Spectrometry: A New Tool For Mass Spectrometry. *J. Chromatogr. A* **2004**, *1058*, 3−19.
(44) Fernandez-Lima, F.; Kaplan, D. A.; Suetering, J.; Park, M. A. Gas-Phase Separation Using A Trapped Ion Mobility Spectrometer. *Int. J. Ion Mobil. Spectrom.* **2011**, *14*, 93.
(45) Hernandez, D. R.; Debord, J. D.; Ridgeway, M. E.; Kaplan, D. A.; Park, M. A.; Fernandez-Lima, F. Ion Dynamics In A Trapped Ion Mobility Spectrometer. *Analyst* **2014**, *139*, 1913−1921.
(46) Mason, E. A. M.; Transport, E. W. Properties Of Ions In Gases. *Transport Properties of Ions in Gases*; John Wiley & Sons, Inc: New York, 1988; pp 1−560.
(47) Jeanne Dit Fouque, K.; Garabedian, A.; Leng, F.; Tse-Dinh, Y-C.; Ridgeway, M.; Park, M.; Fernandez-Lima, F. Trapped Ion Mobility Spectrometry Of Native Macromolecular Assemblies. *Anal. Chem.* **2021**, *93*, 2933−2941.
(48) Liu, F. C.; Kirk, S. R.; Bleiholder, C. On the Structural Denaturation Of Biological Analytes In Trapped Ion Mobility Spectrometry − Mass Spectrometry. *Analyst* **2016**, *141*, 3722−3730.
(49) Garabedian, A.; Butcher, D.; Lippens, J. L.; Miksovska, J.; Chapagain, P. P.; Fabris, D.; Ridgeway, M. E.; Park, M. A.; Fernandez-Lima, F. Structures Of The Kinetically Trapped I-Motif DNA Intermediates. *Phys. Chem. Chem. Phys.* **2016**, *18*, 26691−26702.
(50) Eschweiler, J. D.; Rabuck-Gibbons, J. N.; Tian, Y.; Ruotolo, B. T. CIUsuite: A Quantitative Analysis Package For Collision Induced Unfolding Measurements Of Gas-Phase Protein Ions. *Anal. Chem.* **2015**, *87*, 11516−11522.
(51) Pham, K.; Dhulipala, G.; Gonzalez, W. G.; Gerstman, B. S.; Regmi, C.; Chapagain, P. P.; Miksovska, J. Ca2+ and Mg2+ Modulate Conformational Dynamics And Stability Of Downstream Regulatory Element Antagonist Modulator. *Protein Sci.* **2015**, *24*, 741−751.
(52) Humphrey, W.; Dalke, A.; Schulten, K. VMD: Visual Molecular Dynamics. *J. Mol. Graphics* **1996**, *14*, 33−38.
(53) Phillips, J. C.; Braun, R.; Wang, W.; Gumbart, J.; Tajkhorshid, E.; Villa, E.; Chipot, C.; Skeel, R. D.; Kalé, L.; Schulten, K. Scalable Molecular Dynamics With NAMD. *J. Comput. Chem.* **2005**, *26*, 1781−1802.
(54) Huang, J.; Rauscher, S.; Nawrocki, G.; Ran, T.; Feig, M.; de Groot, B. L.; Grubmüller, H.; MacKerell, A. D., Jr. CHARMM36M: An Improved Force Field for Folded and Intrinsically Disordered Proteins. *Nat. Methods* **2017**, *14*, 71−73.
(55) Essmann, U.; Perera, L.; Berkowitz, M. L.; Darden, T.; Lee, H.; Pedersen, L. G. A Smooth Particle Mesh Ewald Method. *J. Chem. Phys.* **1995**, *103*, 8577−8593.
(56) Camacho, I. S.; Theisen, A.; Johannissen, L. O.; Díaz-Ramos, L. A.; Christie, J. M.; Jenkins, G. I.; Bellina, B.; Barran, P.; Jones, A. R. Native Mass Spectrometry Reveals The Conformational Diversity Of The UVR8 Photoreceptor. *Proc. Natl. Acad. Sci. U.S.A.* **2019**, *116*, 1116−1125.
(57) Lu, H.; Schulten, K. Steered Molecular Dynamics Simulations Of Force-Induced Protein Domain Unfolding. *Proteins: Struct., Funct., Bioinf.* **1999**, *35*, 453−463.
(58) Larriba, C.; Hogan, C. J. Ion Mobilities In Diatomic Gases: Measurement Versus Prediction With Non-Specular Scattering Models. *J. Phys. Chem. A* **2013**, *117*, 3887−3901.
(59) Larriba-Andaluz, C.; Fernández-García, J.; Ewing, M. A.; Hogan, C. J.; Clemmer, D. E. Gas Molecule Scattering & Ion Mobility Measurements For Organic Macro-Ions In He Versus N2 Environments. *Phys. Chem. Chem. Phys.* **2015**, *17*, 15019−15029.
(60) Larriba-Andaluz, C.; Jr, C. J. H. Collision Cross Section Calculations For Polyatomic Ions Considering Rotating Diatomic/Linear Gas Molecules. *J. Chem. Phys.* **2014**, *141*, No. 194107.
(61) Shrivastav, V.; Nahin, M.; Hogan, C. J.; Larriba-Andaluz, C. Benchmark Comparison For A Multi-Processing Ion Mobility Calculator In The Free Molecular Regime. *J. Am. Soc. Mass Spectrom.* **2017**, *28*, 1540−1551.
(62) Schenk, E. R.; Nau, F.; Fernandez-Lima, F. Theoretical Predictor For Candidate Structure Assignment From IMS Data Of Biomolecule-Related Conformational Space. *Int. J. Ion Mobil. Spectrom.* **2015**, *18*, 23−29.
(63) Tien, M. Z.; Meyer, A. G.; Sydykova, D. K.; Spielman, S. J.; Wilke, C. O. Maximum Allowed Solvent Accessibilites Of Residues In Proteins. *PLoS One* **2013**, *8*, No. e80635.

https://doi.org/10.1021/acsomega.1c03744
ACS Omega 2021, 6, 29567−29576